

# Strength of non-spherical particles with anisotropic geometries under triaxial and shearing loading configurations

S. A. Galindo-Torres · D. M. Pedroso · D. J. Williams · H. B. Mühlhaus

the date of receipt and acceptance should be inserted later

**Abstract** This paper presents a study on the macroscopic shear strength characteristics of granular assemblies with three-dimensional complex-shaped particles. Different assemblies are considered, with both isotropic and anisotropic particle geometries. The study is conducted using the Discrete Element Method (DEM), with so-called sphero-polyhedral particles, and simulations of mechanical true triaxial tests for a range of Lode angles and confining pressures. The observed mathematical failure envelopes are investigated in the Haigh-Westergaard stress space, as well as on the deviatoric-mean pressure plane. It is verified that the DEM with non-spherical particles produces results that are qualitatively similar to experimental data and previous numerical results obtained with spherical elements. The simulations reproduce quite well the shear strength of assemblies of granular media, such as higher strength during compression than during extension. In contrast, by introducing anisotropy at the particle level, the shear strength parameters are greatly affected, and an isotropic failure criterion is no longer valid. It is observed that the strength of the anisotropic assembly depends on the direction of loading, as observed for real soils. Finally simulations on a virtual shearing test show how the ve-

locity profile within the shear band is also affected by the grain's shape.

**Keywords** Complex shaped grains · failure criteria · discrete element method

## 1 Introduction

The mechanics of granular media is a current subject of intensive study from both engineers and physicist. Several theoretical models have existed, ranging from elasto-plastic models [1] to more elaborated theories such as hypo-plasticity [2]. Almost all of these theories are built from a common template: a relationship between the stress tensor  $\boldsymbol{\sigma}$  (or stress rate  $\dot{\boldsymbol{\sigma}}$ ) and the current strain tensor  $\boldsymbol{\varepsilon}$  as follows,

$$[\boldsymbol{\sigma}, \dot{\boldsymbol{\sigma}}] = f(\boldsymbol{\varepsilon}), \quad (1)$$

which is true for isotropic materials. However anisotropy, and more specifically cross or vertical anisotropy, is commonly found in geological materials. The origins of this anisotropy are many. For instance, due to geological history, rocks may have internal fractures aligned to a particular direction; or granular assemblies of elongated particles may have a preferential direction of alignment which defines their structure. Regardless of its origin, anisotropy has the same effect on modelling, it changes the fundamental template of Eq. 1 to include a dependence on the coordinate system orientation and makes the problem considerably more complex. Furthermore it introduced non-coaxiality, i.e. the principal systems of the stress and strain tensors are not necessarily aligned.

Considering that the cross anisotropy is always along a preferential direction, defined as the *director* vector  $\mathbf{n}$

---

S. A. Galindo-Torres  
National Centre for Groundwater Research & Training,  
School of Civil Engineering, The University of Queensland,  
Brisbane QLD 4072, Australia

S. A. Galindo-Torres · D. M. Pedroso · D. J. Williams  
Geotechnical Engineering Centre, School of Civil Engineering,  
The University of Queensland, Brisbane QLD 4072, Australia

H. B. Mühlhaus  
Earth System Science Computational Centre, The University  
of Queensland, Brisbane, Australia

in literature [3], the template for constitutive models of cross-anisotropic media is:

$$[\boldsymbol{\sigma}, \dot{\boldsymbol{\sigma}}] = f(\boldsymbol{\varepsilon}, \mathbf{n}). \quad (2)$$

Models based on the director formalism have been successful in describing some feature of the mechanical behaviour of anisotropic rock formations [4,3]. However, finding the correct form of the material parameters for this models is challenging since experimental data is scarcely found in the literature, a problem addressed by Kolymbas *et al* recently [5].

The purpose of this paper is to fill this gap by providing new data, based on DEM simulations for loose granular materials. In this paper, only anisotropy caused by the particle geometry is considered. To achieve this, the Voronoi spheropolyhedra technique, introduced by the authors in a previous work [6] is used. The Voronoi construction allows some control over the particle geometry while still having a random configuration. A similar work was conducted before using the Voronoi construction in 2D by Peña *et al* [7]. However, there are some features of the mechanical behaviour of granular assemblies that can only be studied in 3D situations such as the shape of the failure envelope which will be addressed in this paper.

This paper is structured as follows: In Sec. 2 a brief description of the Voronoi spheropolyhedra method is presented; in Sec. 3 the description of the simulation set-up for a True Triaxial Test (TTT) is shown in Sec. 3 followed by the results obtained for isotropic (Sec. 4) and anisotropic (Sec. 5) samples. Sec. 6 presents some results of virtual shearing test simulations and their dependence on the particle's geometry. Finally, in Sec. 7 the conclusions for this work are presented.

## 2 Methods

Cubic ensembles of particles are mechanically loaded virtually and the resulting deformations are observed. The kinematics and dynamics of each single particle are computationally represented and the macroscopic behaviour is observed. The main innovation of the method employed here is the use of a technique for smoothing the particles, in which all edges have the shape of pharmaceutical pills or capsules. The resulting particles are called spheropolyhedra (see, *e.g.*, [8,9,6,10,11,12]). Basically, all edges are swept by spheres, turning them into capsules, where the radius  $R$  of the sweeping sphere defines the sphero-radius of the particle. The geometry of each particle is defined by a set of vertices, edges, and faces. This technique hugely simplifies the numerical method, since now the contact forces have a unique

definition, contrary to schemes employing polygons or polyhedra (see, *e.g.*, discussion in [6]).

To generate the packing, the Voronoi tessellation method is used as described in the *Voro++* library implemented by C. Rycroft [13]. Once the Voronoi array is obtained, each particle is eroded and dilated by a spherical element of radius  $R$  (the sphero-radius). The result is an array of polyhedral particles with rounded corners and without any initial overlap or voids between them, *i.e.* a close-packing. Fig. 1 illustrates a cubic packing of 10648 Minkowsky-Voronoi spheropolyhedra, which is adopted as the experimental specimen for the numerical simulations of true triaxial tests. In Sec. 5, a method to employ this construction to generate anisotropic specimens is described in detail. For more information on this particle generation method, please refer to [6].

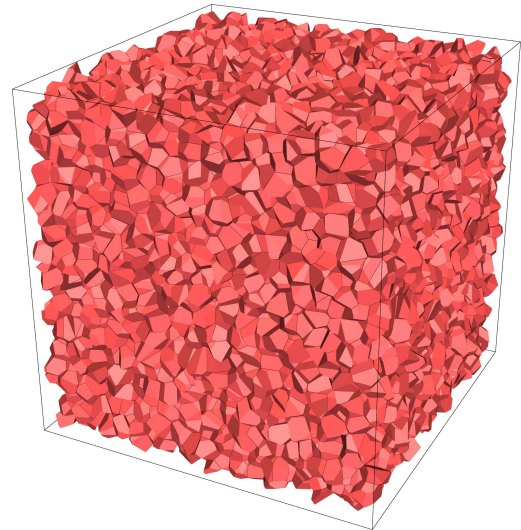


**Fig. 1** Cubic packing with 10648 quasi-general (spheropolyhedra) particles generated by means of the *Voronoi-erosion* technique.

## 3 True triaxial test

To elucidate the form of the relationship between stresses and strains, usually the sample is subjected to different stress configurations and the resulting strains are measured. For this purpose the True Triaxial Test (TTT) is a convenient apparatus to obtain this information. The TTT apparatus is composed by a system of six rigid plates forming a parallelepiped. Because the DEM code employed in this work can handle polyhedral particles, the loading plates of the apparatus are also DEM particles. This is very convenient, since no change to the code is necessary in order to implement the contact between

the loading plates and the granular material representing the specimen. The friction coefficient between the plates and the particles can easily be controlled; here, the friction coefficient is set to zero simulating fully-lubricated walls.

Forces are applied to the plates of the virtual apparatus according to a pre-defined stress path. To calculate the stresses, the cross-sectional areas for each direction are updated as the plates move. Stresses are defined as negative during compression (Classical Mechanics convention). Principal strain components are calculated by the change in the distance between opposite plates divided by their initial separation. The following Continuum Mechanics quantities are calculated:

$$p_{cam} = -\frac{\sigma_x + \sigma_y + \sigma_z}{3} \quad (3)$$

$$q_{cam} = \frac{\sqrt{(\sigma_z - \sigma_x)^2 + (\sigma_x - \sigma_y)^2 + (\sigma_y - \sigma_z)^2}}{\sqrt{2}} \quad (4)$$

$$\varepsilon_v = \varepsilon_x + \varepsilon_y + \varepsilon_z \quad (5)$$

$$\varepsilon_d = \frac{\sqrt{2}}{3} \sqrt{(\varepsilon_z - \varepsilon_x)^2 + (\varepsilon_x - \varepsilon_y)^2 + (\varepsilon_y - \varepsilon_z)^2} \quad (6)$$

Therein,  $\sigma_i$  are the principal stress components, and  $\varepsilon_i$  are the principal strain components,  $p_{cam}$  is the negative of the Cambridge mean stress invariant [14],  $q_{cam}$  is the Cambridge deviatoric stress invariant,  $\varepsilon_v$  is the volumetric strain, and  $\varepsilon_d$  is the deviatoric strain.

To verify the shear strength parameters of cubic assemblies of granular media subject to the combination of three stress components, the stress paths illustrated in Fig. 2 can be applied. These allow the construction of the failure envelopes in the Haigh-Westergaard space. Each path is described as follows:

- (1) Initial confinement of the specimen by means of isotropic stresses;
- (2a) Conventional (cylindrical) compression tests with constant lateral stresses and increasing vertical stress;
- (2b) Conventional (cylindrical) extension tests with constant vertical stress and increasing lateral stresses;
- (3) p-constant tests with a combination of stresses such that a pre-defined constant Lode angle ( $\theta$ ) can be reproduced on the octahedral plane (see Fig. 3). These paths vary from extension ( $\theta = -30^\circ$ ) to compression ( $\theta = +30^\circ$ ).

The Lode angle is illustrated in Fig. 3 and is defined according to the following expression:

$$\theta = 30^\circ - \arctan \left( \frac{\sqrt{3}(\sigma_x - \sigma_y)}{2\sigma_z - \sigma_x - \sigma_y} \right). \quad (7)$$

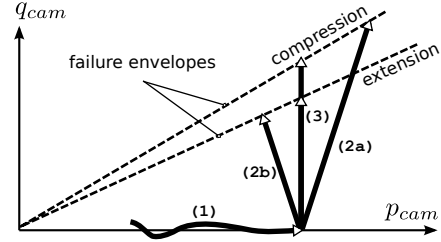


Fig. 2 Applied stress paths.

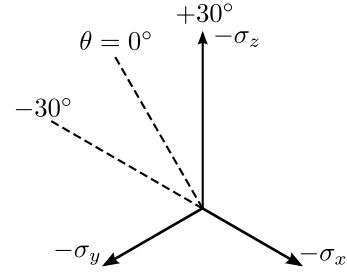


Fig. 3 Octahedral plane and definition of Lode angle  $\theta$ .

Stress-based failure criteria can be defined by observing either the peak or the residual stresses attained in mechanical tests, such as triaxial tests. For instance, the ultimate stresses measured in triaxial tests with increasing deviatoric stresses can be used for this definition. Results from triaxial tests can be used to define failure criteria regarding either the macroscopic friction angle under compression ( $\theta = +30^\circ$ ) or the friction angle under extension ( $\theta = -30^\circ$ ). Only one of these two angles is necessary for a mathematical model. In this paper, the results of friction angles under compression  $\phi_{comp}$  are thus considered. After obtaining this single material parameter, the following criteria are fitted to the simulated data: Mohr-Coulomb (see, *e.g.*, [15]), Matsuoka-Nakai [16], and Lade-Duncan [17].

The Mohr-Coulomb failure criterion predicts a linear relationship between  $q_{cam}$  and  $p_{cam}$  for the stress states at failure and can be mathematically expressed according to (disregarding cohesion):

$$\frac{\sigma_1^* - \sigma_3^*}{\sigma_1^* + \sigma_3^*} = \sin \phi_{comp} \quad (8)$$

Therein,  $\sigma_i^*$  are the sorted (increasing) principal stress values. With this expression, the shear strength under extension will be smaller than that under compression. Therefore, the shape of the Mohr-Coulomb failure envelope is of a deformed hexagon when viewed in the octahedral plane.

The Matsuoka-Nakai [16] failure criterion predicts the same shear strength as the Mohr-Coulomb failure criterion, for both compression and extension. For plane strain or when the Lode angle is in the range  $-30^\circ < \theta < +30^\circ$ , the Matsuoka-Nakai failure criterion predicts

**Table 1** Microscopic constants for the DEM analyses.

Constant	Description
$K_n = 100kN/m$	Contact normal stiffness
$K_t = 50kN/m$	Contact tangential stiffness
$\mu = 0.4$	Microscopic friction coefficient
$g_n = 0.8s^{-1}$	Normal viscous coefficient
$g_t = 0.0s^{-1}$	Tangential viscous coefficient
$\beta = 0.12$	Rolling resistance stiffness coefficient (only for spheres with rolling resistance)
$\eta = 1.0$	Plastic moment coefficient (only for spheres with rolling resistance)

a higher shear strength than the Mohr-Coulomb criterion. The Matsuoka-Nakai failure criterion is directly defined based on the three characteristic invariants  $I_i$  of the stress tensor according to:

$$\frac{I_1 I_2}{I_3} = 9 + 8 \tan^2 \phi_{comp} \quad (9)$$

Another failure criterion similar to the Matsuoka-Nakai failure criterion is the Lade-Duncan [17]. This criterion predicts a higher shear strength under extension than that predicted by the Matsuoka-Nakai or Mohr-Coulomb failure criteria. The Lade-Duncan criterion is given by:

$$\frac{I_1^3}{I_3} = \frac{(3 - \sin \phi_{comp})^3}{(1 + \sin \phi_{comp})(1 - \sin \phi_{comp})^2} \quad (10)$$

#### 4 Results for isotropic specimens

Firstly, the behaviour of cubic assemblies of isotropic granular media is investigated using the DEM code. The applied stress path is the one numbered (3) in Fig. 2, which is enforced after an initial isotropic compression is applied (path (1) in Fig. 2).

Simulations of true triaxial tests are carried out with assemblies of sphero-polyhedra (Fig. 1). The packings are randomly generated as described earlier in this paper. The microscopic constants adopted in all analyses are organised in Table 1. In the following,  $p_{cte}$  means constant  $p_{cam}$ .

Tests with sphero-polyhedra are carried out in order to verify whether the macroscopic shear strength of a cubic packing of particles can be represented by a linear model or not. The linear model here applies to the relationship between deviatoric and mean stresses. The compression ( $\theta = +30^\circ$ ) path with p-constant is employed to represent this.

Results for 10,648 Voronoi particles are shown in Fig. 4, in which it can be observed that a linear fitting can be adopted in order to model these results. The

results are compared with the response of two- sphere assemblies. One is a pure spherical specimen and the other uses the rolling resistance model to represent the effect of shape [18,19,20]. In this paper, the rolling resistance implementation follows the one described in reference [21]. Considering that it is a minor component of this study, only a brief explanation is given herein. In this scheme, the rolling resistance is a fictitious moment applied to the particles that opposes rolling movement. This moment is defined by two constants: the rolling resistance stiffness constant  $\beta$ , which controls the linear grow of the resistance moment with the rolling angle; and the plastic moment coefficient  $\eta$ , which sets a limit to the maximum value for the resistance moment.

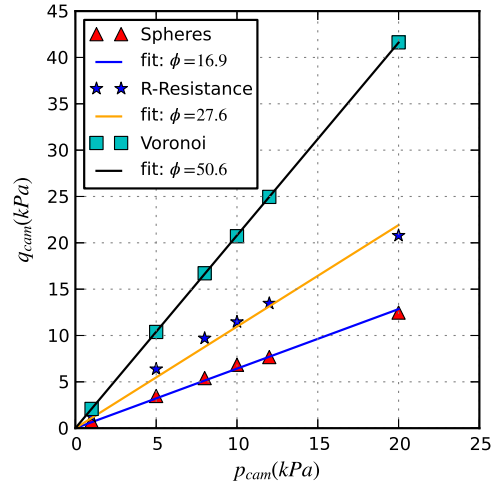


**Fig. 4** Tests with 10000 spheres and 10648 Voronoi particles under compression (path (3) with constant  $p_{cam}$ ).

Geometry plays an important role in the material's friction response. As can be seen, a spherical specimen has a lower shear strength than the Voronoi soil for the same set of parameters. The authors have explored this issue before [6], and several other authors have found independently similar results [22,18,23]. The general consensus is that the rolling of the particles greatly reduces the overall soil shear strength. Non-spherical shapes restrain the particles rolling capabilities and therefore increase the soil shear strength. In fact it has been shown that ideal spheres without rolling resistance can only simulate soils with macroscopic friction angles up to a value of  $20^\circ$  [24,25], regardless of the imposed microscopic friction coefficient, a fact that hinders its ability to reproduce real soils.

The failure envelope for the specimen with rolling resistance lies between the other two. Therefore it is expected that by tuning the rolling resistance coefficients, the Voronoi soil failure envelope can be reproduced with

sphere assemblies. A recent study by Estrada *et al* [26] has shown that indeed rolling resistance can be considered a parametric representation of shape. However, as we will shown later on, this is only valid for isotropic constructions. Obtaining the rolling resistance parameters reproducing the Voronoi particles requires further analysis and should be the subject of future work.

After the initial simulation by compressing the specimens ( $\theta = 30^\circ$ ), further simulations are carried out by changing the Lode angle between  $-30^\circ$  to  $30^\circ$ . In Fig. 5 the results of the stress ratio  $q/p$  as a function of the deviatoric strain  $\varepsilon_d$  for the Voronoi specimen are shown.

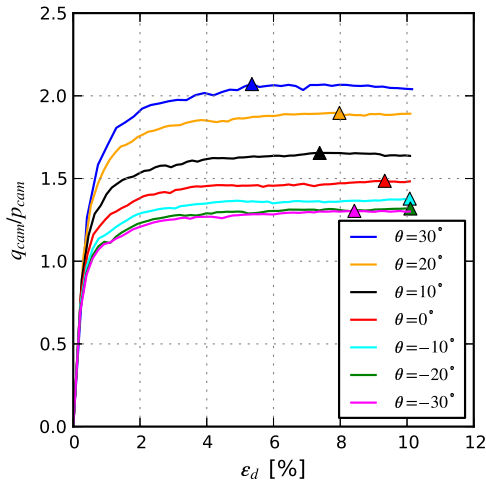


**Fig. 5** Stress ratio as a function of  $\varepsilon_d$  for Voronoi particles.

In compression tests, the packing has a higher shear strength than in extension tests. The reason is that during extension the particles have more space to rearrange and move. This movement controls and reduces the overall shear strength as discussed before. Due to the close packing of the Voronoi construction there is no initial compression of the volume and two adjacent Voronoi particles are prone to start sliding from the beginning, hence with a small  $\varepsilon_d \sim 5\%$  the failure is reached.

The data obtained with DEM simulations of true triaxial tests are now plotted in the Haigh-Westergaard 3D space of principal stresses in Fig. 6. In particular, a view along the hydrostatic axis is considered, with focus on the so-called octahedral plane. This allows the investigation of an appropriated macroscopic failure envelope for isotropic materials. Although the failure envelope is a 3D surface in the Haigh-Westergaard stress space, only its cross-section on the octahedral plane is drawn, for a fixed  $p_{cam}$  value.

For the mathematical definition of a particular failure criteria with linear deviatoric-mean stress relation-

ship, a constant macroscopic friction angle must be defined beforehand. Either the angle at compression or extension can be employed for such task. Here  $\phi_{comp}$  at compression is considered. In the Voronoi specimen, the Lade Duncan fits perfectly for all the considered points. This agrees with Suiker *et al* [22] findings for spherical assemblies and also with experiments on real specimens [17].

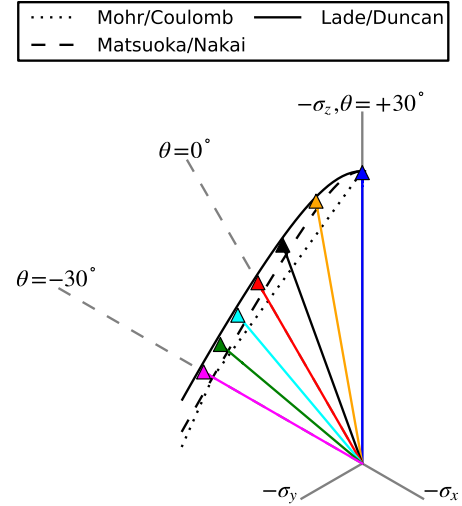


**Fig. 6** Failure envelope in the octahedral plane for Voronoi particles and  $p_{cam} = 10kPa$ .

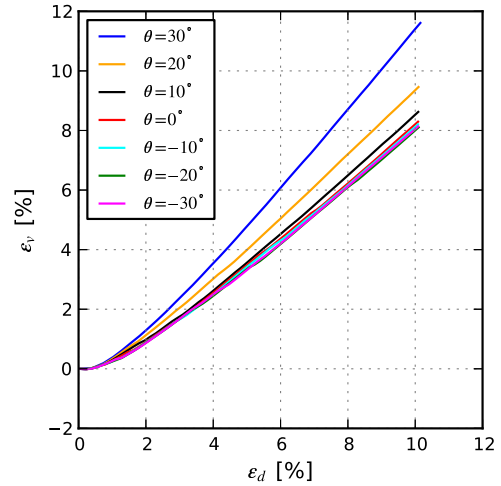


**Fig. 7**  $\varepsilon_v$  versus  $\varepsilon_d$  for the Voronoi particles with  $p_{cam} = 10kPa$ .

Finally, the volumetric evolution of the Voronoi specimen is plotted in Fig. 7. Due to the closely-packed nature of the Voronoi construction, the last specimen



starts to expand from the beginning of loading. In real experiments with sand [27], this volumetric behaviour is similar; however sometimes an initial compression is observed, after which expansion arises. Most sand specimens allow some compression from the beginning. Therefore, real validation should not consider the closely packed Voronoi construction as an initial configuration, but should have an initial sample preparation simulation before the TTT simulation is carried out. For instance, some Voronoi particles could be randomly erased at the beginning to generate some initial voids before the isotropic compression.

## 5 Results for anisotropic specimens

Usually, anisotropy takes the form of cross-anisotropy [28, 29, 30] where it is present in only one direction perpendicular to a plane wherein largely isotropic. This especial direction is commonly parallel to the direction of deposition. If the particles have anisotropic shapes, their deposition will tend to align the particles along principal planes. To reproduce this behaviour we use again the Voronoi construction with a modification to produce an anisotropic array. This method has been used before in 2D and it has been reported that indeed this anisotropy strongly affects the macroscopic friction of the granular specimen [7]. To the best of our knowledge this is the first time that this effect is explored in 3D with the Voronoi construction.

As pointed out in Sec. 2 the isotropic Voronoi tessellation is achieved by having an initial uniform cubic grid where each cell has a unique Voronoi point in a random position. We use the same method by considering more cells along the  $z$  axis. The ratio between the number of cells along  $z$  and the other two directions is defined as the aspect ratio  $\Lambda$ . The cells are still cubic cells before the Voronoi algorithm is applied, and therefore the box is no longer cubic but rectangular with a longer  $z$  length. Once the Voronoi tessellation is obtained, the  $z$  dimensions for each particle are stretched until the desired cubic specimen is obtained. In Fig. 8 several examples of anisotropic Voronoi constructions are shown. The total number of particles  $N_p$  is equal to the total number of cubic cells. In our case  $N_p = n^3 \Lambda$ , where  $n$  is the number of cells along the horizontal dimension. We choose  $n$  so that  $N_p$  is as close as possible to 10000. For instance, for  $\Lambda = 1.0$   $n = 22$  and  $N_p = 10648$ ; while for  $\Lambda = 5.0$   $n = 13$  and  $N_p = 10985$ . Caution should be taken in the construction of anisotropic specimens. If the anisotropy axis  $z$ , called *director* in the literature [31], is not parallel to any of the principal TTT axes, the stress tensor may have shearing components and could not be obtained just with the stresses applied

on the TTT lids. By considering the  $z$  axis as the *director* we may argue that the internal stress tensor and the applied stresses on the TTT apparatus are coaxial.

For the anisotropic specimens the TTT simulation is run for two particular Lode angles  $\theta = 30^\circ$  and  $\theta = -150^\circ$  representing compression and extension along the  $z$  axis respectively. In Fig. 9 the stress ratio  $M = q/p$  is shown for these two Lode angles and five different  $\Lambda$  values. The maximum stress ratio increases with  $\Lambda$  and it reaches an upper limit when  $M = 3.0$ . When this condition is met the pressure is entirely due to  $\sigma_z$  component since  $\sigma_x$  and  $\sigma_y$  are equal to zero, i.e. the stress is align in the  $z$  direction. At this point the lateral apparatus plates have lost contact with the granular specimen.

This highly anisotropic specimen has a maximum strength ( $\phi = 90^\circ$ ) under vertical compression and does not exert any lateral earth pressure. In contrast, for the extension along  $z$  simulations we observe a different effect, the stress ratio decreases with the anisotropy. In this case  $\sigma_z$  decreases gradually given more freedom to the system to be deformed by  $\sigma_x$  and  $\sigma_y$ . These lateral stresses are parallel to the particles principal planes and therefore they can slide easier against their neighbours which explains the lower shear strength.

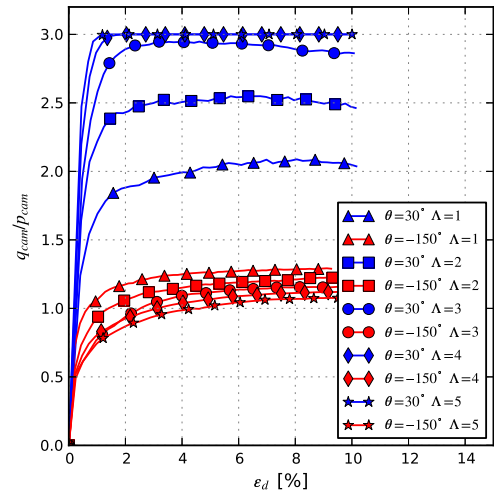


**Fig. 9** Stress ratio  $q/p$  versus  $\varepsilon_d$  for two different Lode angles  $\theta$  and five aspect ratios  $\Lambda$ .

The obtained peak stress ratios  $M = q_{cam}^{peak}/p$  for four Lode angles are shown in Fig. 10. For the compression along the  $z$  axis ( $\theta = 30^\circ$ )  $M$  grows with the increase of the anisotropic ratio  $\Lambda$  until it reaches an upper limit  $M = 3.0$  for  $\Lambda = 4.0$ . This corresponds to a friction angle of  $\phi = 90^\circ$ . Therefore, with this stress configuration a maximum shear strength parameter is found ( $\phi = 90^\circ$ ), unless the particles are allowed to

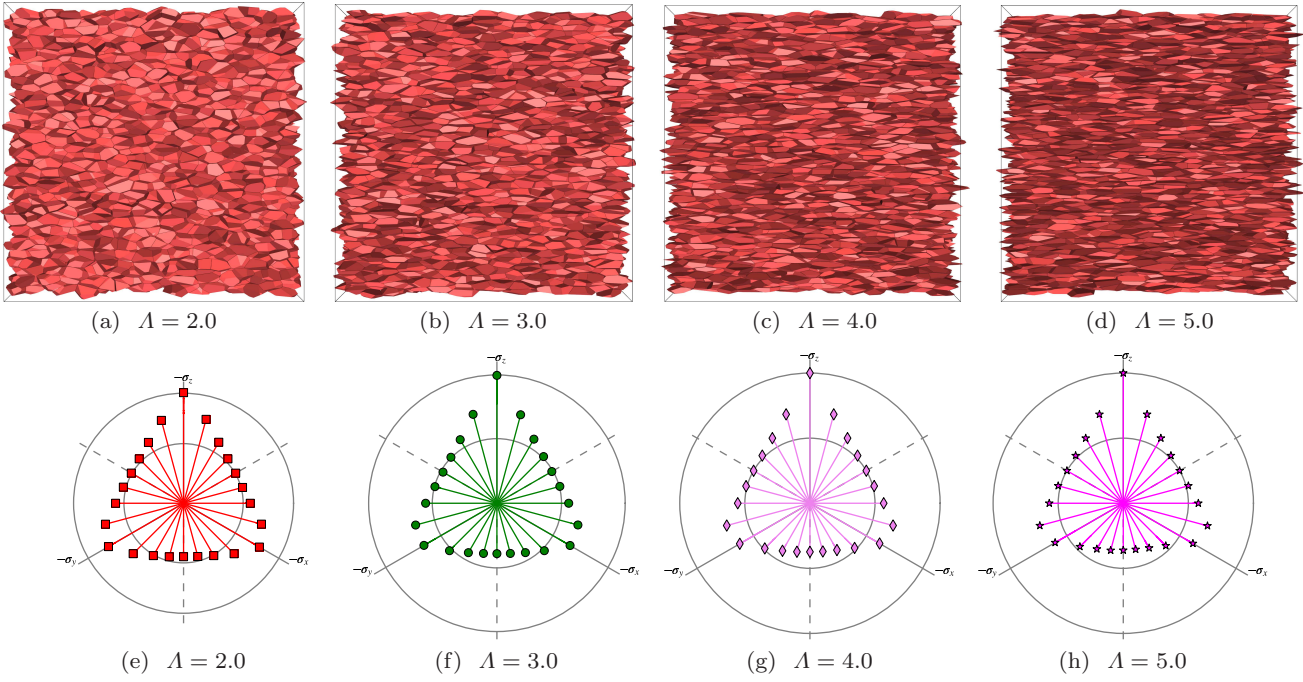


**Fig. 8** (a-d) anisotropic specimens obtained with the Voronoi construction for different values of the aspect ratio  $\Lambda$ . (e-h) the failure surface on the octahedral plane for each one of these specimens, the circles are drawn to aid visualise the anisotropy. The symmetry for each  $60^\circ$  is lost as the specimen becomes more anisotropic, i.e. the shear strength for compression along the vertical axis is different than that along the horizontal axes and the shear strength under extension along the vertical axis is different to that along the horizontal axes.

break which is ignored in the present model. In contrast, for extension along the  $z$  axis ( $\theta = -150^\circ$ ) the shear strength is reduced. Therefore the anisotropic specimen is susceptible to failure when  $\sigma_z$  is reduced with confined conditions. For compression along  $y$  ( $\theta = -90^\circ$ ) the shear strength is gradually reduced while for  $y$  extension ( $\theta = 90^\circ$ ) it is reduced. This is explained by the same argument of the alignment of particles principal planes and the stresses.

The TTT simulations are carried out for the whole octahedral plane, and not just for the  $\theta = -30^\circ, 30^\circ$  section. It has been found that for each third of the circle the constant strain rate should be imposed along different directions. For future reference we used the following simulation programs: for  $\theta = -75^\circ$  to  $30^\circ$  the strain was controlled along the  $x$  axis; for  $\theta = 45^\circ$  to  $150^\circ$  we controlled the  $y$  axis; and for  $\theta = -90^\circ$  to  $165^\circ$  the  $z$  axis.

The simulation results are shown in Fig. 11 for  $\Lambda = 1$  and  $\Lambda = 2$ . It can be seen that the anisotropic failure envelope presents symmetry between the  $x$  and  $y$  direction but it is deformed along the  $z$  direction. For compression along the  $z$  axis ( $\theta = 30^\circ$ ) there is an increase in the shear strength while for extension  $\theta = -150^\circ$  a slight decrease is detected. This cross-anisotropy agrees qualitatively with results obtained in

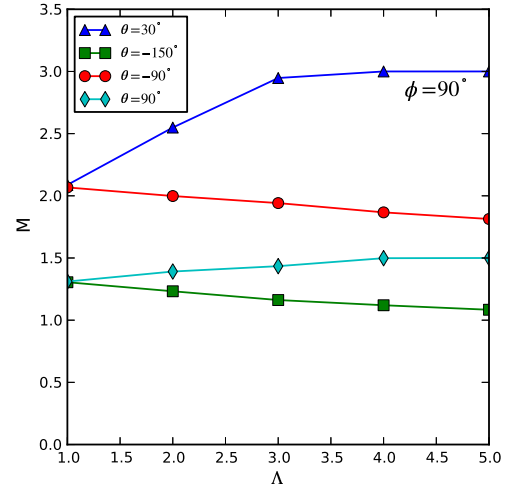


**Fig. 10** Friction angle  $\phi$  as a function of the aspect ratio  $\Lambda$ .

real specimens [28,29,30] where the failure criteria fitted for the compression along the  $z$  axis usually overestimate the shear strength under compressions along the  $x$  and  $y$  axes. This difference between compression along the horizontal axes is even more pronounced as the aspect ratio  $\Lambda$  is increased. This can be further observed in Fig. 8(e-h), where the shear strength under compression along the vertical axis becomes much higher than

that along the horizontal axes, and the shear strength under extension along the vertical axes becomes smaller than that along the horizontal axes.

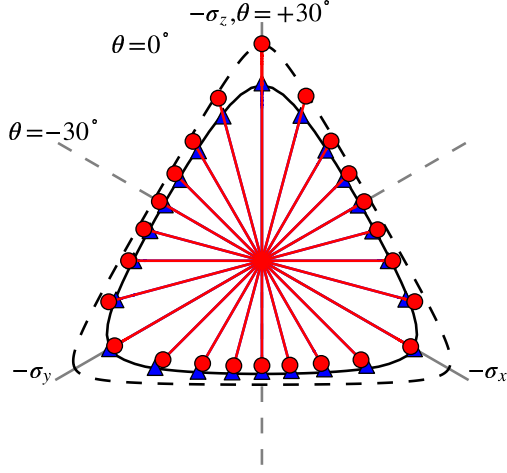


**Fig. 11** Failure envelope in the octahedral plane for the isotropic Voronoi ( $\Lambda = 1$ ) and anisotropic ( $\Lambda = 2$ ) specimens with  $p_{cam} = 10kPa$ . The Lade Duncan failure criterion is fitted for the isotropic specimen (solid line,  $\phi_{comp} = 50.6^\circ$ ) and for the anisotropic specimen (dashed line,  $\phi_{comp} = 62.1^\circ$ ).

In Fig. 11, it can be observed that the anisotropic specimen has a higher shear strength than the isotropic one for all Lode angles, except for values between  $\theta = -90^\circ$  and  $\theta = -210^\circ$  — the “bottom” of the diagram. For this portion, the anisotropic specimens shear strength is slightly lower than that for the isotropic one because the stress is mainly concentrated along the vertical axis and there is a decrease of pressure along the direction parallel to the contact planes. Therefore the particles have slightly more freedom to slide against each than in the isotropic case. On the other hand, vertical compression of the anisotropic specimen is stronger because the particles are extremely constrained against sliding or rolling against their neighbours.

Finally, the volumetric behaviour is shown in Fig. 12 for  $\theta = 30^\circ$  and  $\theta = -150^\circ$  and five values of  $\Lambda$ . For  $\theta = 30^\circ$  all specimens start dilating from the beginning. This is due to the close-packing of the Voronoi construction, as discussed above. This dilatancy is more pronounced as  $\Lambda$  increases. However, this can be explained by the movement of the apparatus plates. As was mentioned before, for  $\Lambda = 5.0$ ,  $M = 3.0$ , which is equivalent to a friction angle of  $\phi = 90^\circ$ , meaning that the specimen does not fail. At this point the lateral stresses are equal to zero. Since the system started from an isotropic compression state, the lateral plates have to expand to reduce the lateral stresses and this expansion explains the high dilatancy. In contrast, for

$\theta = -150^\circ$  there is an initial compression for large values of  $\Lambda$ . In this case, the dilatancy decreases with  $\Lambda$ . Since the particles are almost planar for large values of  $\Lambda$ , they slide parallel to their principal planes, no new voids are produced, and therefore  $\varepsilon_v$  is kept small.

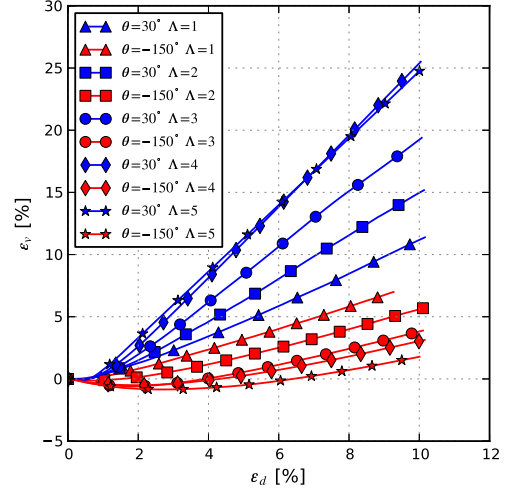


**Fig. 12** Volumetric strain  $\varepsilon_v$  versus  $\varepsilon_d$  for two different Lode angles  $\theta$  and five aspect ratios  $\Lambda$ .

## 6 Shearing test

To further explore the effects of anisotropic grain geometry, simulations inside a virtual shearing test were also carried out. As it is well known, at elevated stress levels the deformation of granular assemblies has the tendency to localize in narrow shear bands [32,33]. Inside the shear band, complex granular kinematics are present, characterised by vortices of particles rolling relative to each other [33,34].

It is commonly accepted that the non-uniform deformation within shear bands is associated with the buckling of the force chains sustaining the load [35]. This buckling is observed mainly in DEM simulations where the column structures can be identified. The shear band simulations are usually carry out with spherical elements [32] but the rolling resistance artefact is introduced to model the effect of shape. Although the rolling resistance is a valid technique to reduce the effect of rotations, as discussed above, it does not represent the effect of interlocking due to shape.

A comparative study of the shearing strength for different Voronoi samples is presented herein. To make a fair comparison, an initial simulation is conducted over the spherical sample with the rolling resistance parameters reported above. The simulation is a shearing



cell with periodic boundary conditions in the horizontal  $x$  direction. The initial container has dimensions of  $L_x = 20\text{cm}$ ,  $L_y = 5\text{cm}$  and  $L_z = 80\text{cm}$  and is filled with an array of 6000 spheres with a uniform random distribution for their radii varying from 0.35 to 0.5cm. The lids perpendicular to the  $z$  direction are kept fixed and are also frictionless. The lids perpendicular to the  $y$  direction are modelled with a triangular pattern to increase roughness, something that is easy to do with the sphero-polyhedra approach. The sample is compressed initially with a pressure of 1kPa applied to the lids across the  $y$  direction. After this compression stage is finished, the triangular lids are moved with a constant velocity in opposite directions to simulate a shearing state. The velocity of the shearing lids is chosen to ensure that the inertial number  $I = \dot{\gamma}d\sqrt{\rho/P}$  ( $d$  the average particles diameter,  $\rho$  the density and  $P$  the pressure) takes a value of  $10^{-5}$  ensuring a quasi static state [36]. Fig 13 shows the shearing test setup for spheres.

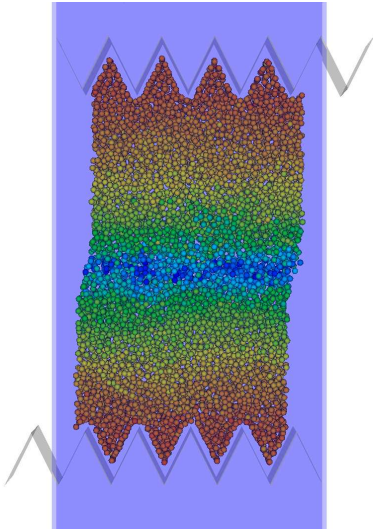


**Fig. 13** Setup for the shearing test over a sample of spherical elements. The colourmap is proportional to the particles velocity

The shearband can be observed in Fig. 13 as a thin band of particles with low relative velocities (blue band). The velocity profile inside the granular medium behaves initially as a linear function of the height. Gradually it becomes S-shaped as the shear strain increases until it reaches a constant profile and a shear band can be identified. This type of displacement profile is in agreement with Cosserat-Continuum theory-based models for simple shear [32]. Fig 14 shows the final velocity profile. A shear band can be identified by the variation of the ve-

locity with the height as shown by the horizontal lines in Fig. 14.

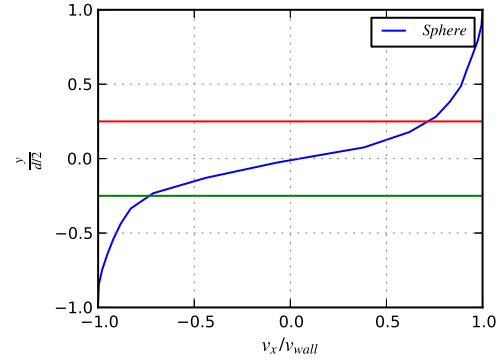


**Fig. 14** Velocity profile (average particle velocity) as a function of the height inside the granular sample. Horizontal lines serve as visual aid to identify the shear band.

The same setup was used for the different Voronoi samples to determine the dependence of the shearing test response on the anisotropy factor  $\Lambda$ . For this case the number of particles was chosen for  $\Lambda = 1$  to be 75% of 8000 particles (6000) distributed over a Voronoi lattice of  $20 \times 80 \times 5$  cells (5 cells along the  $z$  direction). the reason that 25% of the 8000 particles are eliminated is to mitigate the strong effect of the original array interlocking while keeping the original layered structure. Grain anisotropy is now introduced along the  $y$  axis. Fig. 15 shows the shearing cell for two samples with  $\Lambda = 1.0$  and  $5.0$ . It is evident from the colourmap that the velocity profile is not the same as for the spherical soil. Also, although the number of particles is the same, the spherical soil is more compacted (as seen by its height) since the spheres are reduced in size to introduce some randomness.

To find the correct velocity profile, the sample must be sheared gradually until the profile is constant for any further increase of shear. In Fig. 16 shows the profile for several values of  $\gamma$ . As can be seen for a value of  $\gamma = 0.2$  the isotropic sample reaches the steady velocity profile. This is a consistent fact along all the other values for  $\Lambda$  and therefore this limit value for  $\gamma$  was used for the comparative study.

Fig. 17 shows the velocity profile at the steady state for different values of  $\Lambda$ . As can be seen, a shear band is not as easily defined for the Voronoi samples as for the spherical soils. In fact for high values of  $\Lambda$  the velocity profile is almost a linear function of the height. There is no rolling of particles or vorticity, undoubtedly due to the shape preventing relative rotations. In fact, since the particles are flat, they may be considered as layers sliding against each other which explains the lin-

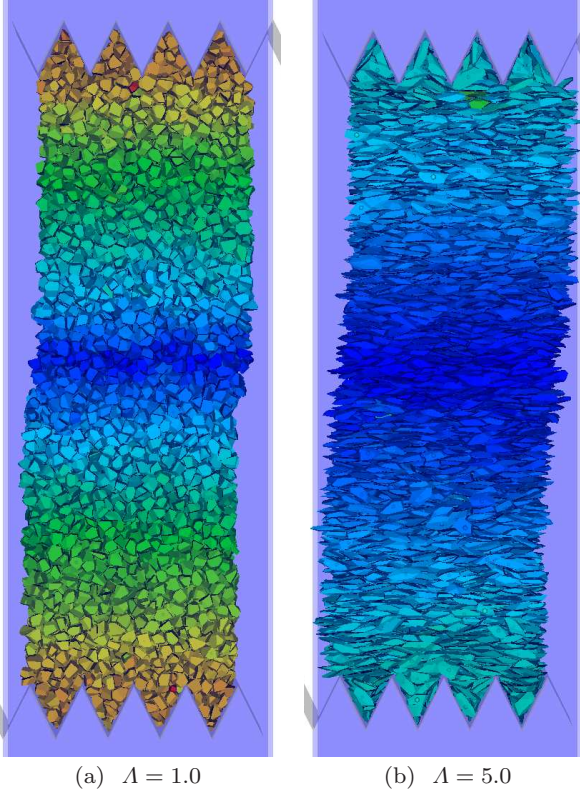


**Fig. 15** Setup for the shearing test over a sample of Voronoi elements for two different values of  $\Lambda$ . The colourmap is proportional to the velocity.

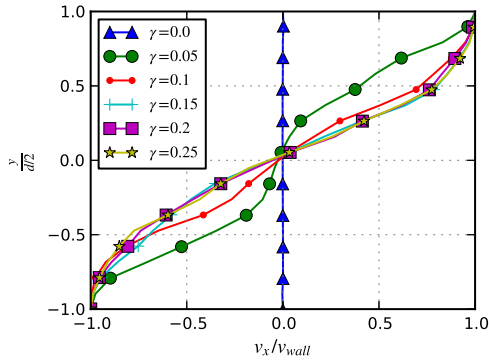


**Fig. 16** Evolution of the velocity profile (average particle velocity) as a function of the height inside the granular Voronoi sample for different values of the shear  $\gamma$  for  $\Lambda = 1.0$ .

ear dependence. This has strong consequences specially in issues such as the Heat Flux Paradox [34] which was a disagreement between the heat predicted by simple shear models and the one measured during the shear produced by earthquakes. In the simple shear models the velocity field inside the shear band is assumed to be linear, and hence a significant number of particles are sliding against each other, increasing the heat output. On the other hand, when the velocity profile is S-shaped

and vortices are present at the middle, the produced heat is significantly lower due to the small number of particles actually sliding. The difference between the heat output of both profiles is discussed in [37]. Herein we have provided numerical evidence that the preference of one velocity profile over the other is related to the shape of the particles inside the shear band.

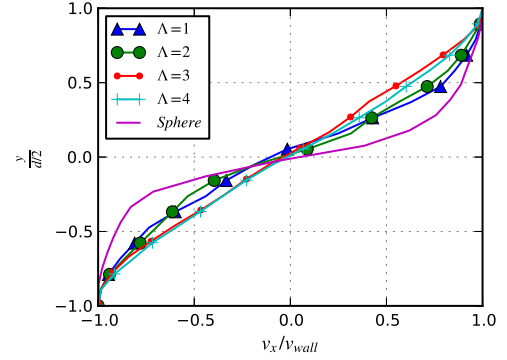


**Fig. 17** Velocity profile, at the steady state, as a function of the height inside the granular Voronoi sample for different values of  $\Lambda$  and for the spherical geometry.

Finally, the shear stress is also presented for the different Voronoi soils. Fig. 18 shows the shear stress measured over the lids for different values of  $\Lambda$ . Layered structures associated with higher  $\Lambda$  values are easier to slide and hence offer less resistance to shear while the isotropic structure offers the maximum shear stress. The reason is the same as for the election of a velocity profile discussed above, in the isotropic cases the particles have to roll against each other to produce relative displacement while for highly anisotropic samples the particles slide easily.

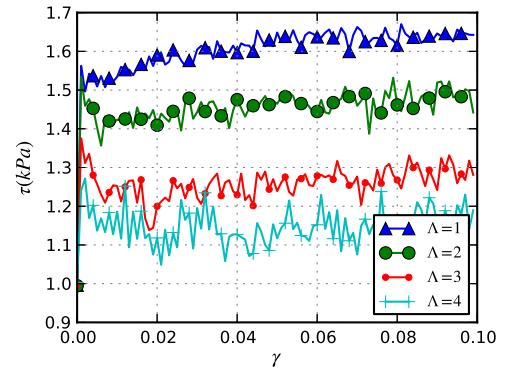


**Fig. 18** Shear stress vs.  $\gamma$  produced over the bottom and top lids for different values of  $\Lambda$ .

## 7 Conclusions

The Voronoi sphero-polyhedra scheme presented herein can be used to study the effect of particle shape with a more sophisticated approach than the rolling resistance models previously used. The results of simulations are presented for Voronoi sphero-polyhedra. In this paper, both isotropic and anisotropic random Voronoi specimens are considered. As an extension to the original work of Suiker *et al* [22], it has been found that the isotropic Voronoi sphero-polyhedra failure envelope is well-fitted by the Lade Duncan model. The Voronoi construction ensures only expansion at the shearing stage due to its closely-packed nature. The macroscopic friction angle can reach values as high as  $50^\circ$ , which are impossible to achieve for spheres without rolling resistance. Considering that there is experimental evidence of such high friction angles in sand specimens, it may be concluded that the individual geometry of the particles plays a larger role than initially thought.

Also, it has been found that the failure envelope is strongly affected by particle anisotropy. By inducing anisotropy at the particles geometry, a deformed failure envelope with cross-anisotropy, as observed in real soils and reported in the literature [28, 29, 30], has been reproduced.

It has been observed that a strong inherent particle anisotropy can theoretically produce packings that have a maximum strength ( $\phi = 90^\circ$ ) when the loading is parallel to the direction in which the geometric anisotropy is induced (the *director* axis). Therefore their bearing capacity is infinite and the exerted lateral earth pressure is zero. In contrast, when the stress configuration is mainly on the horizontal, the specimen is actually weaker than the isotropic one and prone to failure for lower values of the deviatoric stress  $q$ .

A final analysis was done over the results obtained from a shearing test simulation with periodic boundary conditions. It has been observed in this and previous studies that the velocity profile inside the shearband follows a S-shaped behaviour [38, 39, 32]. In this study, numerical results are presented showing how this velocity profile under steady shearing conditions is also affected by the particle's geometry. In fact while the Cosserat Continuum based models predict these S-shaped patterns, simpler models assumed linear velocity profiles. Herein it has been shown that the selection of one velocity profile over the other depends on the particles' shape. Moreover, the shape anisotropy has been shown to also affect the measure shear strength of the material as an extension on the results obtained with the triaxial test simulations.

Further studies, with different specimen preparation methods should be carried out. A deposition simulation under gravity should be carried out prior to the triaxial test simulation, to observe if after deposition the shear strength parameters presented in this paper are still valid. Other effects such as tapping and shaking should be introduced as well. If after these simulations the particles' principal planes are still aligned, it is expected that the measured shear strength parameters are the same as the ones reported herein.

## References

1. R. Scott, in *Constitutive Equations for Granular Non-cohesive Soils* (Balkema, 1988), pp. 723–726
2. J. Tejchman, E. Bauer, *Computers and Geotechnics* **19**(3), 221 (1996)
3. H. Mühlhaus, L. Moresi, M. Cada, *Pure and Applied Geophysics* **161**(11), 2451 (2004)
4. H. Mühlhaus, F. Dufour, L. Moresi, B. Hobbs, *International Journal of Solids and Structures* **39**(13), 3675 (2002)
5. D. Kolymbas, P. Wagner, A. Blioumi, *International Journal for Numerical and Analytical Methods in Geomechanics* (2010)
6. S.A. Galindo-Torres, D.M. Pedroso, *Phys. Rev. E* **81**(6), 061303 (2010). DOI 10.1103/PhysRevE.81.061303
7. A. Peña, R. Garcia-Rojo, H. Herrmann, *Granular Matter* **9**, 279 (2007). URL <http://dx.doi.org/10.1007/s10035-007-0038-2>
8. F. Alonso-Marroquin, *EPL (Europhysics Letters)* **83**(1), 14001 (2008). DOI 10.1209/0295-5075/83/14001
9. S.A. Galindo-Torres, F. Marroquin, Y. Wang, D.M. Pedroso, J. Castaño, *Physical Review E* **79**(6) (2009)
10. L. Pournin, M. Weber, M. Tsukahara, J.A. Ferrez, M. Ramaioli, T.M. Liebling, *Granular Matter* **7**(2-3), 119 (2005)
11. L. Pournin, T. Liebling, in *Powders & Grains 2005* (Balkema, Leiden, 2005), pp. 1375–1478
12. L. Pournin, On the behavior of spherical and non-spherical grain assemblies, its modeling and numerical simulation. Ph.D. thesis, École Polytechnique Fédérale de Lausanne (2005)
13. C.H. Rycroft, To appear in 'Chaos' (2009). URL <http://math.lbl.gov/voro++>
14. A. Schofield, P. Wroth, *Critical State Soil Mechanics* (McGraw Hill, 1968)
15. R.O. Davis, A.P.S. Selvadurai, *Plasticity and Geomechanics* (Cambridge, United Kingdom, 2002)
16. H. Matsuoka, T. Nakai, in *Proc. JSCE* (1974), 232, pp. 59–70
17. P.V. Lade, J.M. Duncan, *Journal of Soil Mechanics and Foundations Division (ASCE)* **99**(10), 793 (1973)
18. N. Estrada, A. Taboada, F. Radjai, *Phys. Rev. E* **78**(2), 021301 (2008). DOI 10.1103/PhysRevE.78.021301
19. M. Jiang, H.S. Yu, D. Harris, *Computers and Geotechnics* **32**(5), 340 (2005). DOI 10.1016/j.compgeo.2005.05.001
20. K. Iwashita, M. Oda, *Journal of Engineering Mechanics ASCE* **124**(3), 285 (1998)
21. N. Belheine, J.P. Plassiard, F.V. Donzé, F. Darve, A. Seridi, *Computers and Geotechnics* **36**(1-2), 320 (2009). DOI 10.1016/j.compgeo.2008.02.003

22. A.S.J. Suiker, N.A. Fleck, *Journal of Applied Mechanics* **71**(3), 350 (2004). DOI 10.1115/1.1753266
23. E. Azéma, F. Radjai, *Phys. Rev. E* **81**(5), 051304 (2010). DOI 10.1103/PhysRevE.81.051304
24. A. Suiker, N. Fleck, *Journal of applied mechanics* **71**, 350 (2004)
25. S. Galindo-Torres, D. Pedroso, *Physical review. E, Statistical, nonlinear, and soft matter physics* **81**(6 Pt 1), 061303 (2010)
26. N. Estrada, E. Azéma, F. Radjai, A. Taboada, *Phys. Rev. E* **84**, 011306 (2011). DOI 10.1103/PhysRevE.84.011306. URL <http://link.aps.org/doi/10.1103/PhysRevE.84.011306>
27. T. Nakai, *Soils and Foundations* **29**(1), 119 (1989)
28. G. Mortara, *International Journal for Numerical and Analytical Methods in Geomechanics* **34**(9), 953 (2010). DOI 10.1002/nag.846
29. Z. Gao, J. Zhao, Y. Yao, *International Journal of Solids and Structures* **47**(22-23), 3166 (2010). DOI 10.1016/j.ijsolstr.2010.07.016
30. M.M. Kirkgard, P.V. Lade, *Canadian Geotechnical Journal* **30**(4), 848 (1993)
31. H. Mühlhaus, L. Moresi, B. Hobbs, F. Dufour, *Pure and Applied Geophysics* **159**(10), 2311 (2002)
32. X. Liu, A. Papon, H. Mühlhaus, *Philosophical Magazine* **92**(28-30), 3501 (2012)
33. S. Galindo-Torres, J. Muñoz, F. Alonso-Marroquín, *Physical Review E* **82**(5), 56713 (2010)
34. F. Alonso-Marroquín, I. Vardoulakis, H.J. Herrmann, D. Weatherley, P. Mora, *Phys. Rev. E* **74**, 031306 (2006)
35. A. Tordesillas, J. Peters, B. Gardiner, *Int. J. for Num. and Anal. M. in Geomechanics* **28**(10) (2004)
36. G. MiDia, *Eur. Phys. J. E* **14**, 341 (2004)
37. S. Galindo-Torres, A. Lizcano, J. Muñoz, *Physical Review E* **86**(6), 061302 (2012)
38. S. Masson, J. Martinez, *Journal of engineering mechanics* **127**(10), 1007 (2001)
39. P. Jop, Y. Forterre, O. Pouliquen, *Nature* **441**(7094), 727 (2006)